Photoacoustics 22 (2021) 100245

Contents lists available at ScienceDirect

Photoacoustics

journal homepage: www.elsevier.com/locate/pacs

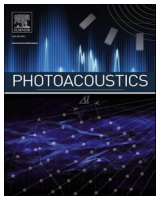

Polyacrylamide hydrogel phantoms for performance evaluation of multispectral photoacoustic imaging systems

Ali Hariri [a], Jorge Palma-Chavez [a], Keith A. Wear [b], T. Joshua Pfefer [b], Jesse V. Jokerst [a,c,d,*], William C. Vogt [b,*]

[a] Department of NanoEngineering, University of California San Diego, La Jolla, CA 92093, USA
[b] Center for Devices and Radiological Health, U.S. Food and Drug Administration, Silver Spring, MD 20993, USA
[c] Department of Radiology, University of California San Diego, La Jolla, CA 92093, USA
[d] Materials Science and Engineering Program, University of California San Diego, La Jolla, CA 92093, USA

ARTICLE INFO

Keywords:
Tissue-mimicking material
Tissue Phantoms
Polyacrylamide
Image quality
Standardization

ABSTRACT

As photoacoustic imaging (PAI) begins to mature and undergo clinical translation, there is a need for well-validated, standardized performance test methods to support device development, quality control, and regulatory evaluation. Despite recent progress, current PAI phantoms may not adequately replicate tissue light and sound transport over the full range of optical wavelengths and acoustic frequencies employed by reported PAI devices. Here we introduce polyacrylamide (PAA) hydrogel as a candidate material for fabricating stable phantoms with well-characterized optical and acoustic properties that are biologically relevant over a broad range of system design parameters. We evaluated suitability of PAA phantoms for conducting image quality assessment of three PAI systems with substantially different operating parameters including two commercial systems and a custom system. Imaging results indicated that appropriately tuned PAA phantoms are useful tools for assessing and comparing PAI system image quality. These phantoms may also facilitate future standardization of performance test methodology.

1. Introduction

Photoacoustic imaging (PAI) is a rapidly emerging technique for mapping light absorption by hemoglobin and deoxyhemoglobin to produce images of vascular morphology and blood oxygen saturation [1]. PAI has shown great potential to provide new functional and molecular imaging biomarkers for many clinical applications including breast cancer detection, oximetry, and surgical guidance, as well as for preclinical research [2–7]. Different imaging applications often require substantially different system designs, which has resulted in a wide variety of system designs described in the literature or currently being sold for preclinical research applications. However, it is unclear how best to objectively and quantitatively evaluate a particular device design and assess its suitability for a given application. There is an outstanding need for well-validated and standardized performance test methods that are suitable for evaluating performance of many types of PAI devices.

Tissue-simulating phantoms play a critical role in medical imaging system development and image quality assessment and often form the foundation of consensus test methods established for mature medical imaging modalities such as ultrasound [8,9]. Such test methods enable device design optimization, calibration, constancy testing, quality management systems, regulatory decision-making, and accreditation programs. One key challenge for PAI is the need for tissue mimicking materials (TMMs) that simultaneously possess optical properties and acoustic properties that are tunable over a biologically relevant range. An ideal phantom would also accurately mimic tissue over a broad range of optical wavelengths and acoustic frequencies. Unfortunately, many materials described in the literature are characterized over a narrower acoustic frequency range (~1−10 MHz) while PAI systems are available over a broader range (~1−40 MHz). Notably, current IEC standards for ultrasound phantom test methods limit their scope to devices operating over 1−15 MHz [8]. Phantoms described in the literature are also often tailored to a specific instrument and may not be suitable for a wide range of different PAI device designs or configurations, which may hamper device intercomparison and result in duplication of effort among researchers and device developers. The availability of phantoms based on well-characterized TMMs suitable for many device designs would provide investigators, instrument manufacturers, and regulatory agencies

* Corresponding authors.
E-mail addresses: jjokerst@ucsd.edu (J.V. Jokerst), william.vogt@fda.hhs.gov (W.C. Vogt).

https://doi.org/10.1016/j.pacs.2021.100245
Received 5 October 2020; Received in revised form 9 December 2020; Accepted 12 February 2021
Available online 20 February 2021

with well-validated tools to assess device performance.

Performance evaluation of PAI devices has been conducted using many materials including ex vivo tissue [10–12]; lipid emulsions such as Intralipid [13]; hydrogels such as gelatin [14], agar/agarose [15–20], and polyvinyl alcohol (PVA) [21]; polyvinyl chloride-plastisol (PVCP) [22,23]; paraffin gel wax [24,25]; and styrene-ethylene/butylene-styrene copolymers [26]. Ex vivo tissue is generally undesirable for standardized image quality test methods due to its variable properties and morphology, heterogeneity, poor reproducibility, and short shelf life. Intralipid is commonly used in optical phantoms but possesses lower acoustic attenuation than tissue [27]. Hydrogel-based TMMs offer easy preparation and fabrication, tunable composition, and good dopant miscibility but typically suffer from poor shelf life and low mechanical strength. PVA cryogels with adjustable stiffness and turbidity can be formed through repeated freeze-thaw cycling. However, the optical and acoustic properties cannot be tuned independently, and slow dye migration from solid inclusions has been reported [28]. Elastomers such as polyurethane or polydimethylsiloxane (PDMS) have been used for ultrasound imaging phantoms, but some of these materials may not accurately mimic the acoustic properties of soft tissues [26,29]. Recently, promising non-aqueous materials have been specifically developed as photoacoustic TMMs such as gel wax [25] and polyvinyl chloride plastisol (PVCP) [30–32]. These materials have been shown to possess relatively high mechanical strength and optical tunability, and acoustic tunability has been demonstrated in PVCP for breast-mimicking formulations. However, the acoustic properties of these TMMs at higher frequencies (e.g., $>$ 15 MHz) have not been reported and may be more highly attenuating than some soft tissues other than breast. These materials also typically require high preparation temperatures, potentially limiting compatible dopant options.

Polyacrylamide (PAA) is a hydrogel that has been used previously for ultrasound phantom TMMs, including in Zerdine® (CIRS, Inc., Norfolk, VA), a commercially available TMM [33]. PAA offers simple preparation, short curing times, low viscosity (thus good dopant miscibility), reduced bacterial infiltration [34], and longer shelf life. PAA may also provide greater mechanical strength and robustness than agar/gelatin hydrogels due to the use of cross-linking polymerization instead of a thermal gelation process. A high degree of optical and acoustic tunability is expected [35–38]. While the acrylamide polymerization reaction is exothermic, PAA has lower preparation temperatures than PVCP and gel-wax phantoms. Like other hydrogels, PAA is still subject to desiccation and should be sealed to maximize product lifetime. While concerns have been raised regarding toxicity of potential residual acrylamide monomer [35], this risk is mitigated through proper safety procedures during production and appropriate design of sealed phantom housings. PAA blocks have been used in photoacoustic contrast agent studies, but the phantom optical and acoustic properties were not adjusted to provide biologically relevant background [39,40]. To the best of our knowledge, PAA has not been used to build image quality phantoms suitable for PAI.

Our overall goal is to develop stable, well-characterized, tunable, and biologically relevant phantoms with broad tunability for a wide array of PAI devices. To this end, our study objectives were to develop and characterize PAA as a new photoacoustic TMM, construct PAA image quality test phantoms, and demonstrate phantom utility through image quality testing of three different PAI systems.

2. Methods and materials

Given the wide variety of PAI applications, TMMs for PAI should offer highly tunable optical and acoustic properties in order to adequately mimic different specific tissues or to represent generic tissue-like conditions. Most photoacoustic TMM development has focused on producing phantoms with biologically relevant optical absorption coefficient (μ_a), optical reduced scattering coefficient (μ_s'), speed of sound (c_s), and acoustic attenuation coefficient (α) [31]. In this study, we aimed to produce a TMM with broad optical and acoustic tunability and to mimic a generic soft tissue. The target μ_a and μ_s' values at 800 nm were 0.1 cm^{-1} and 10 cm^{-1}, respectively, which are generally similar to soft tissues [41]. The target c_s was 1540 m/s as taken from ultrasound standards [8,42]; however, selecting an appropriate target α was challenging due to the wide range of transducer frequencies employed by the PAI systems tested in this study. To ensure phantoms were biologically relevant, yet not overly attenuating at higher frequencies (beyond our current characterization equipment's range), we chose a target α of 0.2 dB/cm/MHz.

2.1. Polyacrylamide preparation

Polyacrylamide (PAA) hydrogels are formed through crosslinking copolymerization of acrylamide and N,N'-methylene bisacrylamide in aqueous solution [43]. A 40 % w/v acrylamide solution containing 19:1 acrylamide:bisacrylamide (AM9024, Thermo Fisher Scientific, Inc., Waltham, MA) was diluted in deionized water, and ammonium persulfate (APS) solution (A7460, Sigma-Aldrich, Inc., St. Louis, MO) was added to initiate the polymerization. The solution was degassed in a steel vacuum chamber for 1 h and then N,N,N',N'-tetramethylethylenediamine (TEMED, Sigma-Aldrich) was added to accelerate free radical formation from APS. TEMED was used within 10 months of purchase. The PAA solution was then mixed, immediately poured into phantom molds, and cured at room temperature for 1 h, with solidification occurring within 5 min. Phantoms were manually tumbled during curing to minimize gravitational settling of dopants [44,45].

2.2. TMM characterization

To evaluate the acoustic property tunability of PAA, acoustic properties were first measured in samples with varying acrylamide concentration of 8–20 % w/v. The base PAA hydrogel does not impart significant acoustic scattering, and thus we increased acoustic attenuation and backscattering by doping 12 % w/v acrylamide samples with soda lime glass beads at concentrations of 0−10 mg/mL (38−63 μm diameter, Potter Industries LLC, Malvern, PA). This ensures that the phantoms are also suitable for bimodal ultrasound and photoacoustic imaging [46,47]. PAA acoustic properties were characterized using a broadband through-transmission substitution technique [48,49] in a tank containing deionized, degassed water. This technique has been previously validated against time-delay spectrometry measurements [50]. PAA samples were cured in nontreated tissue cell culture flasks (08-772-1J, Thermo Fisher Scientific) as shown in Fig. 1A. Flasks were placed in a water bath between a pair of co-axially aligned broadband transducers (A313S-SU, Olympus, Inc., Waltham, MA) with one transducer acting as a transmitter and the other as a detector. Both transducers had 15 MHz center frequencies and 0.63 cm diameters. Transducers were connected to a pulser/receiver (Panametrics 5900PR, Olympus) and received ultrasound signals were digitized at 2.5 GHz using an oscilloscope (MDO3054, Tektronix, Inc., Beaverton, OR). An average of 512 measurements was taken at each of 4−6 locations per sample. Group velocity in the sample, c_s, was calculated as

$$c_s = \frac{c_w}{1 + \frac{\Delta t}{\Delta x} c_w} \tag{1}$$

where c_w is the speed of sound in water, Δt is the transit time delay between the two measurements, and Δx is the flask thickness. The acoustic attenuation coefficient vs. frequency, $\alpha(f)$ in dB, was calculated as

$$\alpha(f) = \frac{10}{\Delta x} \log\left(\frac{P_w(f)}{P_s(f)}\right) \tag{2}$$

where $P_s(f)$ is the power spectrum measured through a PAA-filled flask and $P_w(f)$ is the acoustic power spectrum measured in a water-filled

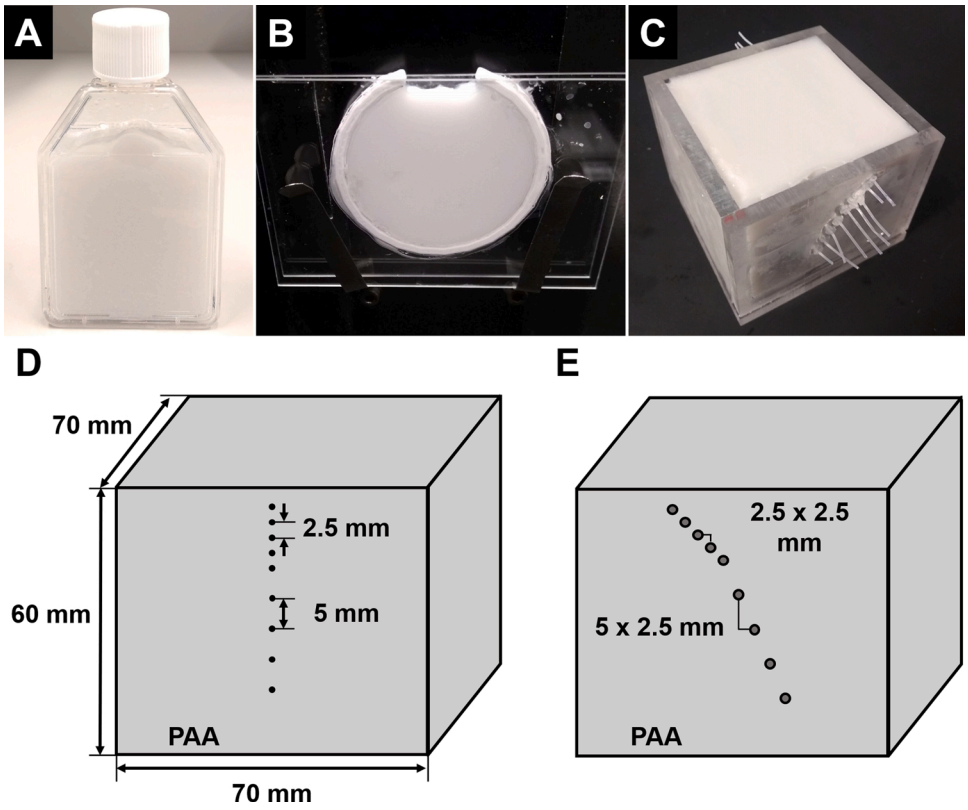

Fig. 1. PAA gels were cured in (A) nontreated tissue cell culture flasks and (B) C-shaped molds glued between a pair of glass slides for acoustic and optical characterization, respectively. Photograph of the penetration phantom (C). Schematics of the resolution phantom containing a column of 50 μm-diameter nylon filaments (D) and penetration phantom containing an array of ink-filled tubes (0.56 mm inner diameter, 0.71 mm outer diameter) (E). Imaging was performed from the top surface in each phantom.

flask. This approach cancels out acoustic transfer characteristics of the flask walls, assuming that differences in acoustic impedances between the gel and water were small enough that differences in transmission coefficients could be neglected. For example, for a gel sample in water, if the differences in c_s and density between gel and water are less than 7% and 20 %, respectively (both true in these experiments), then it can be shown the product of intensity transmission coefficients at both interfaces exceeds 95 % [51]. Attenuation coefficient spectra were fitted to the power-law relationship $\alpha(f) = \alpha_0 f^n$ over the range from 6−18 MHz where α_0 and n are fitting parameters.

To characterize acoustic backscattering, ultrasound images of PAA samples with varying glass bead concentrations were acquired using FDA's custom PAI system (see Section 2.6). Mean image amplitude was measured over a 12 mm x 15 mm (width by height) region of interest (ROI) and compared against similar measurements in a commercial tissue-mimicking ultrasound phantom (Model 040GSE, CIRS, Inc.) [31]. Image acquisition and display settings were fixed for both phantoms.

To produce phantoms with biologically relevant optical properties over a broad range of wavelengths, PAA was doped with India ink (Super black India ink, Speedball Art Products Co., Statesville, NC) and anatase titanium dioxide (TiO_2, 232033, Sigma-Aldrich). These dopants are commonly used in both optical and PAI phantoms, including hydrogels [52,53]. These TiO_2 particles have an average diameter of 550 nm in water [31]. Samples comprising 12 % w/v PAA were doped with 0.004 – 0.010 % v/v India ink or 0.4–1.2 mg/mL TiO_2. Samples were prepared in C-shaped molds with 38.4 mm diameter and 2.5 mm thickness, which were glued between a pair of 75 mm x 50 mm x 1 mm glass slides with an assumed refractive index of 1.5 (Fig. 1B). Total transmittance and diffuse reflectance of samples were measured over 400−1100 nm using an integrating sphere spectrophotometer (Lambda 1050, PerkinElmer, Waltham, MA). μ_a and μ_s' were calculated from these data using the inverse adding-doubling (IAD) algorithm [54]. Sphere measurements were calibrated using a Spectralon 99 % reflectance standard (Labsphere, Inc., North Sutton, NH), and transmittance and reflectance baselines were measured following the IAD manual [55]. Sample thickness was measured using digital calipers with 0.02 mm resolution, subtracting the thickness of the glass slides. The 2.5 mm sample thickness is appropriate for IAD and consistent with previous studies [56,57]. Because unaccounted light losses can cause IAD to overestimate absorption, μ_a values were calibrated against a 12 % PAA sample with 2 mg/mL TiO_2 but no ink, which was assumed to have absorption equal to that of water [58]. Sample scattering anisotropy factor and refractive index were assumed to be 0.9 and 1.34, respectively. Varying anisotropy factor from 0 to 0.9 in a representative PAA dataset varied μ_a (800 nm) and μ_s' (800 nm) by ± 3% and ± 2%, respectively. PAA refractive index at 589 nm has been reported as 1.35 [59], and may be slightly lower in the NIR assuming normal dispersion similar to water [58]. Varying refractive index from 1.33 to 1.35 led to changes in μ_a (800 nm) and μ_s' (800 nm) of ± 5% and ± 0.2 %, respectively.

Ideally, image quality phantoms should offer high mechanical durability and stability of intrinsic properties over time. We prepared optical and acoustic characterization test samples as described above and measured their optical or acoustic properties at 1 day, 8 weeks, and 12 weeks post-fabrication. Optical stability was measured in a set of six 12 % w/v PAA samples each containing 0.7 mg/mL TiO_2 and 0.0045 % v/v India ink. Acoustic stability was measured in a set of seven 12 % w/v PAA samples containing 0−10 mg/mL glass beads to assess dependence of stability on potential glass bead settling. All samples were stored at room temperature and pressure. Samples were weighed at each measurement timepoint to monitor mass loss over time. Average and standard deviation of sample mass, optical properties, and acoustic properties was computed per timepoint, and comparisons between timepoints were made using student's *t*-test.

2.3. Phantom imaging and image analysis

To demonstrate utility of PAA phantoms, we sought to evaluate image quality of three PAI instruments using phantoms formed in 7cm ×

7cm x 6 cm acrylic molds (Fig. 1C). We constructed two image quality phantoms: 1) a "resolution" phantom intended to quantify axial and lateral spatial resolution, and 2) a "penetration" phantom intended to quantify maximum depth of visualization. The resolution phantom contained a column of 50 μm diameter black nylon monofilament sutures (Teleflex Medical OEM, Gurnee, IL) at depths of 5−35 mm (Fig. 1D). The penetration phantom contained an array of light-wall polytetrafluoroethylene tubes (Component Supply Co., Sparta, TN) at depths of 5−35 mm (Fig. 1E). In both phantoms, the first five targets in depth were spaced closer together to ensure a sufficient number of targets in the field of view for high-frequency PAI systems, while the deeper targets were more sparse to cover low-frequency systems. Tubes were filled with India ink solutions with three different μ_a values of 8 cm^{-1}, 4 cm^{-1}, and 2 cm^{-1}. Here, 4 cm^{-1} represents the expected μ_a of hemoglobin at 800 nm (an isosbestic point) for a total hemoglobin concentration of 13.9 g/dL, which is within the normal ranges for adult males (13.5–17.5 g/dl) and females (12–16.0 g/dl) [60]. A value of 2 cm^{-1} thus represents a low-contrast scenario such as anemia (~7 g/dl) while 8 cm^{-1} represents a high-contrast scenario such as using a contrast agent. PAA phantoms were fabricated from a 400 mL batch of solution using a final recipe of 12 % w/v acrylamide, 0.08 % w/v APS, 0.2 % v/v TEMED, 0.7 mg/mL TiO_2, 0.00225 % v/v India ink, and 6 mg/mL glass beads. Phantoms took approx. 5 min to solidify and were allowed to cure for 1 h, with a maximum surface temperature of 46 °C as measured by an infrared thermometer.

We used these PAA phantoms to conduct a multi-site phantom-based image quality assessment of three different PAI systems including a custom system located at FDA and two commercial systems at UCSD [31,61,62]. Fig. 2 shows transducer and light delivery geometries for each system. The custom system combines an optical parametric oscillator (OPO) delivering 5 ns pulses at 10 Hz pulse repetition rate, 690−950 nm tunable wavelength, and 8–10 mJ/cm^2 radiant exposure (Phocus Mobile, Opotek Inc., Carlsbad, CA) with a 128-channel ultrasound acquisition system (Vantage 128, Verasonics Inc., Seattle, WA). PAI was performed with a 7 MHz linear array transducer covered in aluminum foil and placed in contact with the imaging surface (L11−4v, Verasonics) and a 5 mm x 40 mm elliptical optical beam aligned adjacent to the transducer. The foil reduces light absorption at the transducer face, which generates unwanted photoacoustic image clutter. Image reconstruction was performed using a proprietary pixel-oriented delay and sum algorithm from Verasonics [63], and images were pulse energy-compensated using an internal energy meter.

UCSD's available systems included an AcousticX (CYBERDYNE Inc., Japan) and a Vevo LAZR (FUJIFILM VisualSonics, Inc., Ontario, Canada). The AcousticX performs optical excitation using high-density arrays of high-power light-emitting diodes (LEDs) attached to either side of a 10 MHz linear array transducer. LED output has adjustable pulse duration (50−150 ns) and pulse repetition rate (up to 4 kHz). Several swappable LED arrays are available in various wavelengths or pairs of wavelengths; in this study we used 850 nm LED arrays. Image reconstruction was performed using built-in Fourier transform analysis. The Vevo LAZR is an OPO-based system delivering 4−6 ns pulses at 20 Hz repetition rate, 680−970 nm tunable wavelength. Several linear-array transducers are available at different center frequencies (15, 21, 30, and 40 MHz), and each transducer includes an integrated housing containing optical fiber bundles. Preliminary phantom measurements indicated poor target detectability in phantoms using the 21, 30, and 40 MHz probes (data not shown), possibly due to higher acoustic scattering of PAA. Thus, phantom imaging was performed only using the 15 MHz probe (LZ201) in this study (Table 1).

While the three PAI systems have different configurations and software settings, we developed a general set of imaging guidelines intended to standardize data collection across systems. Transducers were coupled to the phantom with ultrasound gel and aligned such that target filaments or tubes were normal to the image plane. Energy was set to maximum output, and imaging was performed at 850 nm. Images were acquired at five locations in each phantom following ultrasound test method recommendations [64]. At 850 nm, the radiant exposures for the custom and Vevo systems measured with a 3.5 mm aperture were approximately 8.0 ± 0.4 mJ/cm^2 and 8.6 ± 0.3 mJ/cm^2, respectively. The AcousticX output was set to maximum energy at 4 kHz, which produced a radiant exposure of 28 ± 0.2 $\mu J/cm^2$ measured with a 12 mm aperture (a larger aperture was needed to measure lower pulse energies). For penetration phantom imaging, the tube array was filled sequentially with India ink solutions with $\mu_a = 2$, 4, or 8 cm^{-1}. Channels were rinsed with water between solutions. Reconstruction speed of sound was fixed at 1540 m/s for all systems.

Imaging phantoms were constructed at FDA, weighed, and then

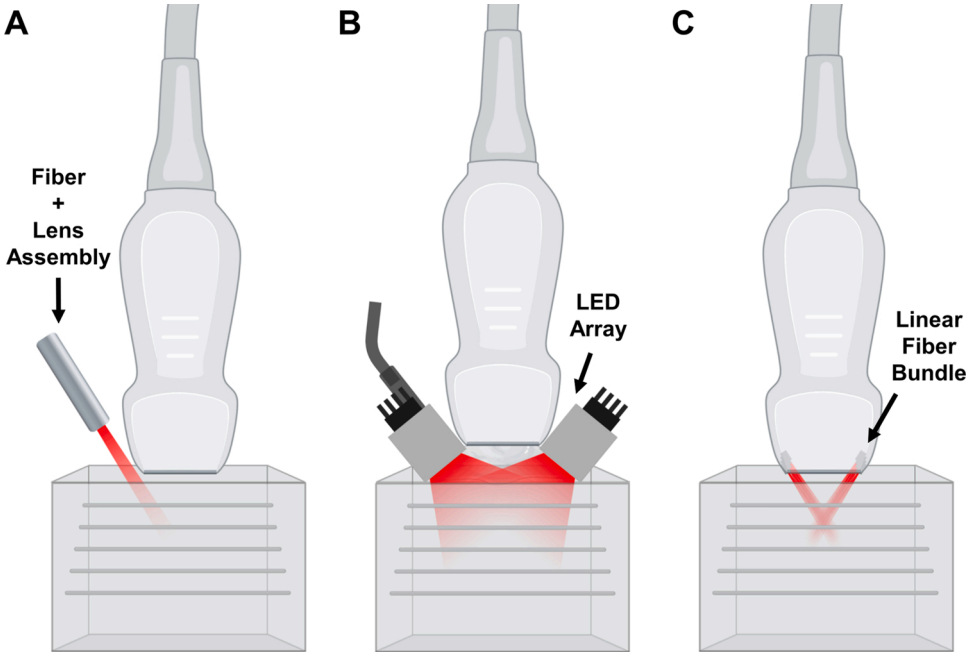

Fig. 2. Schematics of transducer and light delivery geometries for the (A) custom system, (B) AcousticX, and (C) Vevo LAZR.

Table 1
Operating parameters of the three PAI systems.

	Center Frequency, Bandwidth (MHz)	Array Length (mm)	Elevational Focus (mm)	Pulse Repetition Rate (Hz)	Radiant Exposure at 850 nm (mJ/cm^2)
Custom system	7.5, 7	38.4	20	10	8.0
AcousticX	10, 8	38.4	15	4000	0.028
Vevo LAZR	15, 9	32	18	20	8.6

imaged using the custom PAI system. Phantoms were packaged in sealed plastic bags and delivered to UCSD by commercial passenger air transport (i.e., stored in the passenger cabin to avoid possible temperature and pressure differences in the cargo hold). On arrival, phantoms were inspected for damage and weighed to check for desiccation during shipment. Imaging was then performed on the AcousticX and Vevo LAZR systems following the same data acquisition protocol used with the custom system.

Photoacoustic images are typically log compressed to reduce dynamic range of the data and thus improve image visualization by a human reader. However, user-adjustable display settings such as display dynamic range, gain, time-gain compensation, log compression, and thresholding can change image content and thus affect image quality metrics. In this study we evaluated both the preprocessed image data (referred to here as linear amplitude images) and the processed, log-compressed 8-bit images (referred to as displayed images). Following recommendations from ultrasound image quality standards, we selected display settings such that images were not saturated and background was not clipped, and kept display settings fixed during image quality analysis [9,42].

To quantify spatial resolution, a 2 × 2 mm rectangular region of interest (ROI) was drawn over each imaged filament target in linear amplitude images. Vertical and horizontal amplitude profiles intersecting with the maximum amplitude pixel within the ROI were used to calculate the axial and lateral resolution based on the full width at half maximum (FWHM) or -6 dB width [64]. To evaluate maximum imaging depth, 1 × 1 mm ROIs were drawn over tube targets and equal-sized background ROIs were drawn 2 mm to the right of each target. Image quality metrics including signal-to-noise ratio (SNR), contrast-to-noise ratio (CNR), signal-to-background ratio (SBR), and contrast ratio (CR, in dB) for each target using either the linear amplitude image, A, or the displayed image, D. These metrics may be written as:

$$\begin{aligned} SNR_{linear} &= \frac{A_t}{\sigma_{A,b}} \quad CNR_{linear} = \frac{A_t - A_b}{\sigma_{A,b}} \\ SNR_{disp} &= \frac{D_t}{\sigma_{D,b}} \quad CNR_{disp} = \frac{D_t - D_b}{\sigma_{D,b}} \\ SBR_{linear} &= \frac{A_t}{A_b} \quad CR_{linear} = 20\log_{10}\left(\frac{A_t}{A_b}\right) \\ SBR_{disp} &= \frac{D_t}{D_b} \quad CR_{disp} = \frac{DR}{255}(D_t - D_b) \end{aligned} \tag{3}$$

where A_t and D_t are average target ROI values, A_b and D_b are average background ROI values, $\sigma_{A,b}$ and $\sigma_{D,b}$ are standard deviations of the background ROI values, and DR is the display dynamic range in dB [22,42,65,66]. Some correlations are evident between these metrics. For example, CR_{disp} is expected to be similar to CR_{linear} because its definition inverts the linear lookup table that converts log-compressed image data to 0–255 pixel values. Also, given values of any two of SNR, CNR, and SBR, the third metric may be determined via the following relationship:

$$CNR = SNR\left(1 - \frac{1}{SBR}\right) \tag{4}$$

This relationship also illustrates how CNR captures both the effects of target contrast through SBR and background variation through SNR. Despite these correlations, our intent was to evaluate and compare results to determine the most appropriate use of these metrics.

3. Results

3.1. TMM properties

The acoustic properties of the various PAA formulations are shown in Fig. 3. Both c_s and α significantly increased with acrylamide concentration. Acoustic attenuation was linear with PAA concentration up to 16 % PAA ($R^2 > 0.97$), with 20 % PAA samples having higher attenuation than expected from a linear fit. PAA hydrogels with very high acrylamide concentration became significantly stiffer, but these samples were also less homogenous as evidenced by hazy streaks and interfaces. This heterogeneity may be due to uneven heating and crosslinking during the exothermic polymerization reaction [37,38]. As expected, α increased with glass bead concentration, but c_s did not significantly change (data not shown). Therefore, we could tune c_s by varying acrylamide concentration, then tune α by varying glass bead concentration. PAA samples doped with glass beads produced significant acoustic backscattering as seen in the B-mode ultrasound images (Fig. 4). Quantitative analysis of ultrasound images indicated that PAA with a glass bead concentration of 6 mg/mL produced similar ultrasound image amplitudes as the commercial reference phantom. This concentration was much lower than that used in previous PVCP phantoms [31], which may be due acoustic attenuation in PVCP, greater acoustic mismatch between the particle and medium, or differences in particle aggregation. Based on acoustic characterization experiments, we selected a formulation comprising 12 % w/v acrylamide and 6 mg/mL glass beads for further phantom development.

The μ_a and μ_s' spectra of PAA hydrogels were readily tuned using India ink and TiO_2 (Fig. 5). A high degree of linearity of optical properties with respect to dopant concentration was observed for both India ink and TiO_2. These curves were used to fine-tune PAA to match targeted property values. As expected, India ink produced relative flat μ_a spectra except for the increased absorption due to water absorption above 925 nm. TiO_2 produced μ_s' spectra showing a monotonic decrease with wavelength.

PAA samples measured over time showed good resistance to desiccation with no statistically significant mass loss after 8 weeks and <1% mass loss over 12 weeks. This may be attributed in part to the samples being stored in airtight containers needed for water bath immersion in acoustic characterization experiments. This housing approach is consistent with commercial hydrogel phantom designs that typically use a thin plastic membrane or "acoustic window" to seal the hydrogel from the environment but allow high ultrasound transmission through the imaging surface. After 12 weeks, there was a small but statistically significant decrease in speed of sound of 4.1 ± 1.2 m/s (0.2 ± 0.07 %). Acoustic attenuation was highly stable, with α at 10 MHz decreasing by 0.02 ± 0.038 dB/cm (1.4 ± 2.8 %) over 12 weeks. These variations are within acoustic property tolerances recommended in the ultrasound standard IEC 61391−1:2017 (± 10 %) [8]. Optical properties showed greater variation, but no significant trends were observed with time. At 12 weeks, μ_a was 11 ± 1.6 % lower (averaged over 700–950 nm), and μ_s' was 0.2 ± 1.8 % lower. This variation may be partly attributed to uncertainty in the integrating sphere measurements and the IAD calculations.

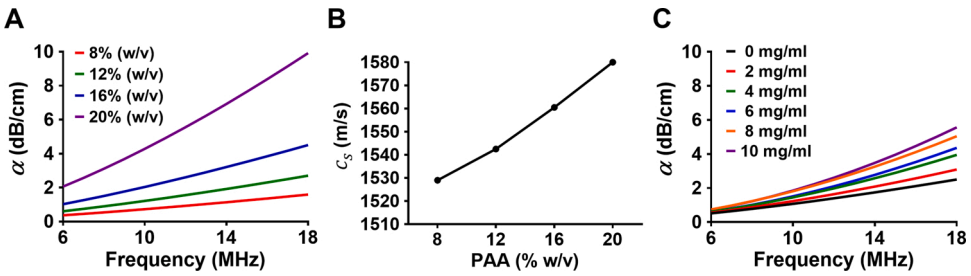

Fig. 3. Effect of PAA concentration on α (A) and c_s (B). (C) shows α for various glass blead concentrations. Error bars omitted for clarity; typical standard deviations for c_s and α were < 1 m/s and $< 5\%$, respectively.

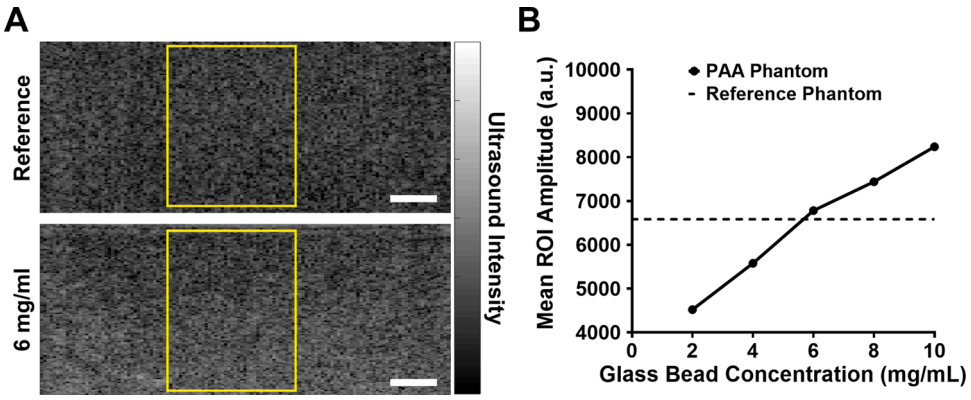

Fig. 4. (A) Ultrasound images of the CIRS reference phantom and PAA sample with 6 mg/mL glass beads. Yellow boxes denote measurement ROIs. Scale bars = 5 mm. (B) Mean ROI amplitude vs. glass bead concentration compared to the reference phantom (dotted line). (For interpretation of the references to colour in this figure legend, the reader is referred to the web version of this article).

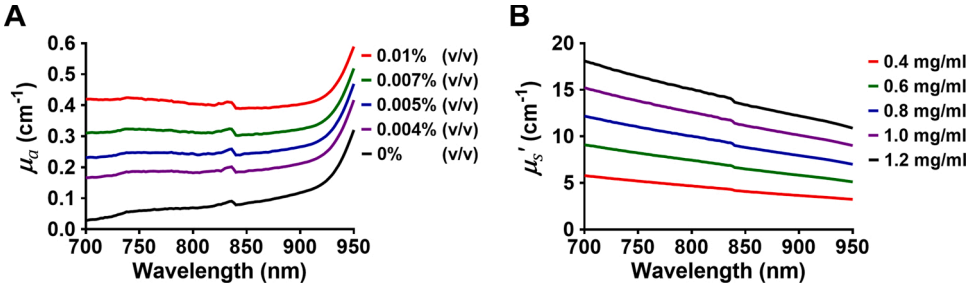

Fig. 5. PAA μ_a (A) and μ_s' (B) spectra as a function of India ink and TiO_2 concentration, respectively. Discontinuities at 840 nm are due to spectrophotometer switching between visible and near-infrared detectors and slits.

3.2. Image quality

Resolution phantom results with the three PAI systems are shown in Fig. 6. Field of view varies between systems due to differences in transducer standoff distance from the phantom surface, as well as acoustic receive data sampling limitations. Axial and lateral FWHM measurements were generally constant with target depth, indicating proper image reconstruction and focusing (Fig. 6D and 6E). FWHM values increased and became noisy for deeper targets, which is due to loss of contrast. As shown in Fig. 6D, axial resolution improved with increasing transducer center frequency (and thus bandwidth), with depth-averaged values of 0.320 mm (custom system, 7 MHz), 0.245 mm (AcousticX, 10 MHz), and 0.148 mm (Vevo, 15 MHz). This trend is expected because axial resolution is primarily determined by transducer bandwidth [30].

Unexpectedly, the opposite trend was observed for lateral FWHM measurements, with lateral FWHM increasing with transducer center frequency (Fig. 6H). Lateral resolution will generally depend on acoustic aperture length and wavelength as well as adequate focusing settings, such as optimal selection of reconstruction speed of sound. Per our imaging protocol, reconstruction speed of sound was locked at 1540 m/s for consistency, rather than allowing user adjustment during testing. However, the measured lateral FWHM for the Vevo LZ201 transducer of 0.52–0.81 mm was consistent with our previous measurements using a line-pair target (0.59–0.75 mm), indicating good agreement between point spread function and bar chart approaches [61,62]. The higher acoustic scattering of PAA at high frequencies may have also affected resolution performance. Finally, the 100 μm-thick plastic acoustic window is on the order of the Vevo system's axial resolution and may have caused focusing aberrations. Reflections due to this membrane are also present in the AcousticX and Vevo images because they operate with a standoff distance (unlike the custom system).

Representative images of the penetration phantom for each PAI system and target absorption level are shown in Fig. 7. These images as shown are optimized for image quality analysis, not human readability, which explains the stronger background and apparent lower image

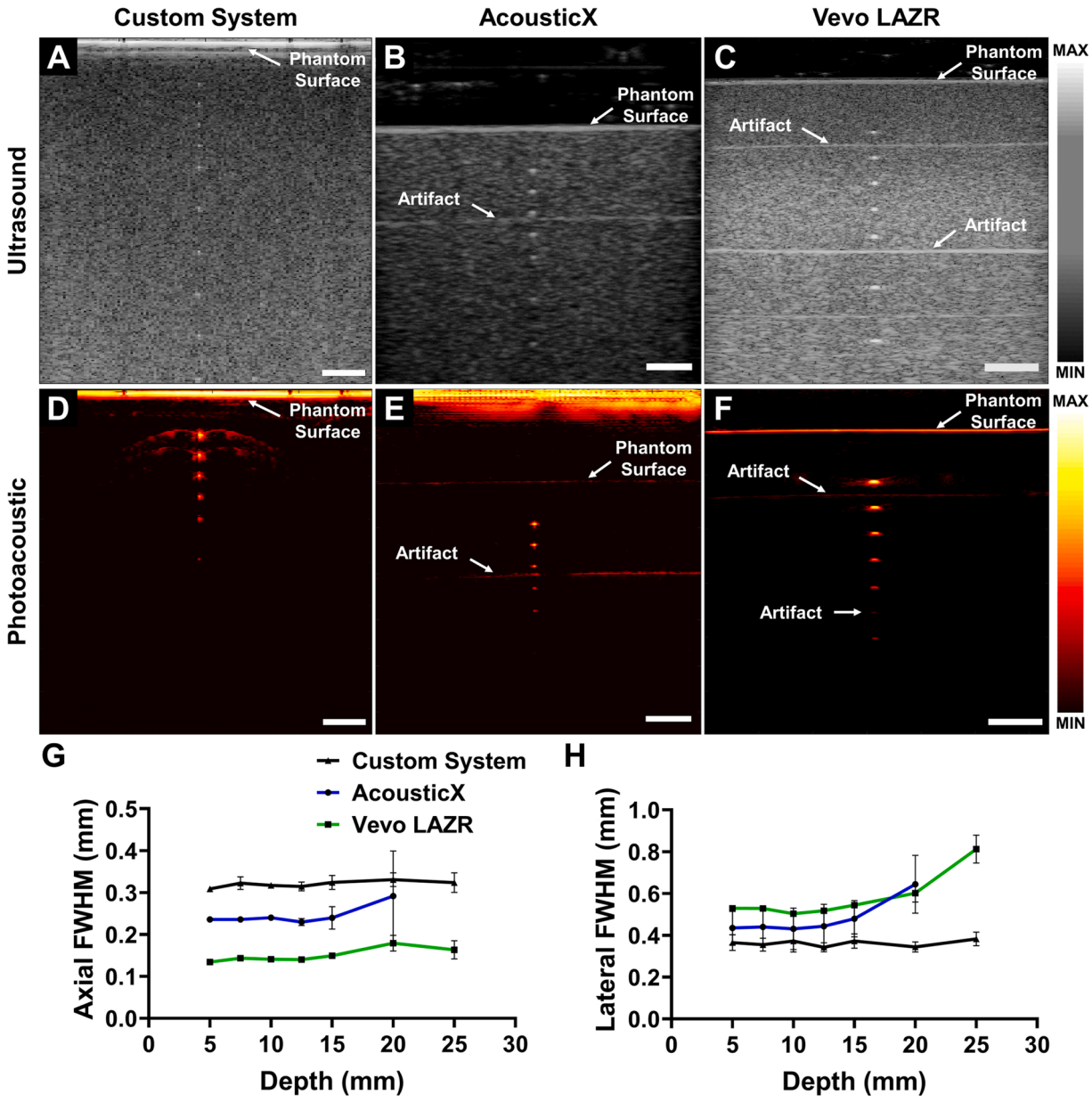

Fig. 6. Representative ultrasound and photoacoustic images of the resolution phantom using the custom system (A, D), AcousticX (B, E), and Vevo LAZR (C, F). Measured axial (G) and lateral (H) FWHM vs. depth for each system. Scale bars = 5 mm. Display dynamic range: custom system (US = 80 dB, PAI = 40 dB), AcousticX (US = 70 dB, PAI = 35 dB), Vevo LAZR (US = 70 dB, PAI = 45 dB).

contrast. Generally, clear qualitative differences in imaging depth were observed across systems and target μ_a. Several artifacts were present in the images. The custom system produced near-field clutter due to optical absorption at the transducer/phantom interface while the AcousticX and Vevo systems, which operate with the transducer above the phantom surface at some standoff distance, produced horizontal line reflection artifacts. Reflection artifacts were also seen beneath tubes; both artifacts are likely due to photoacoustic signals generated at the transducer surface traveling downward and reflecting off the phantom surface or tubes, which doubles the time of flight and the resulting depth determined by image reconstruction.

Image quality metrics computed on linear amplitude images are shown in Fig. 8. SNR_{linear} was omitted as trends vs. depth were similar to those of CNR but with slightly higher values (per Eq. 4). CR_{linear} produced a log-linear decrease with depth because, unlike other metrics, it is expressed in dB (and is also the expression of SBR_{linear} in dB). The custom system had the highest values for all metrics although the curves plateaued for shallow targets as clutter reduced contrast and increased background variation. This pattern may be also be attributed to the in-plane fluence distribution caused by an adjacent beam geometry, which has a somewhat flatter distribution over depths of 0–1 cm, while the other systems may have produced exponential fluence distributions directly beneath the beam [67]. As expected, metrics increased with target μ_a, although this increase was not always linear.

As shown in Fig. 9, choice of display dynamic range strongly impacted overall image appearance and computed image quality metrics. This is expected based on similar effects in ultrasound image quality assessment, and optimal adjustment of display settings clearly should impact image quality. Qualitative inspection showed target detectability generally increased with decreasing display dynamic range especially for deeper targets. As display dynamic range decreased, B and σ approached zero due to background thresholding, thus causing CNR_{disp} and SBR_{disp} to increase (approaching infinity). Following standardized ultrasound test method recommendations, we attempted to minimize

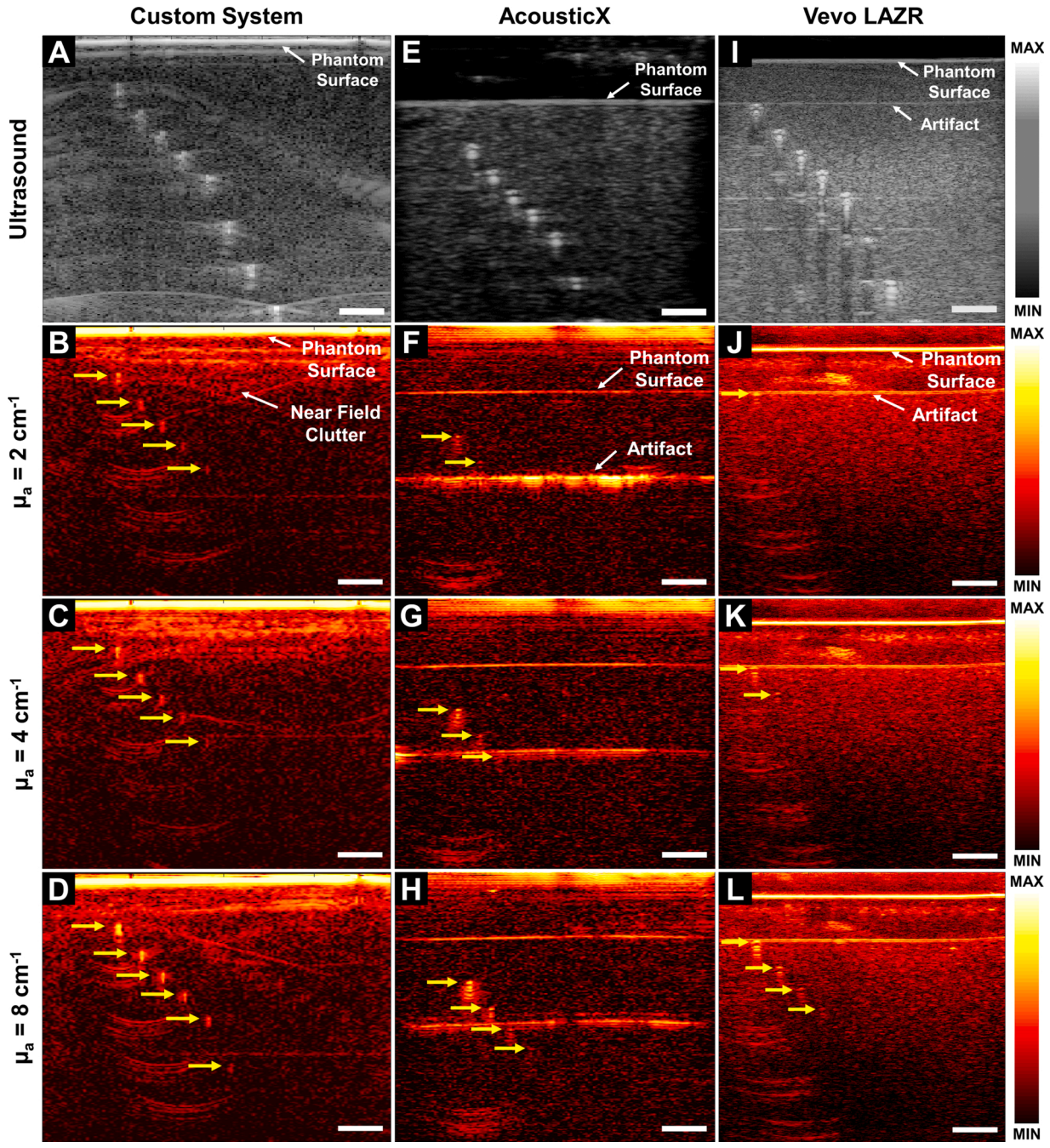

Fig. 7. Ultrasound and photoacoustic images of penetration phantom filled with India ink solutions at μ_a = 8 cm^{-1}, 4 cm^{-1}, or 2 cm^{-1}, acquired by the custom system (A-D), AcousticX (E-H), and Vevo LAZR (I-L). Yellow arrows denote visible targets. Scale bars = 5 mm. Display dynamic range: custom system (US = 80 dB, PAI = 50 dB), AcousticX (US = 70 dB, PAI = 33 dB), Vevo LAZR (US = 70 dB, PAI = 36 dB). (For interpretation of the references to colour in this figure legend, the reader is referred to the web version of this article).

this effect by selecting image display settings in subsequent analyses such that the background was still visible [42,64]. The sensitivity of CNR_{disp} and SBR_{disp} to display settings may suggest correlation with expected human reader performance, and image quality assessment research has generally focused on metrics that consider background variance such as *SNR* and *CNR* [68]. CR_{disp} was relatively insensitive to changes in display dynamic range, which implies this metric may be less appropriate for predicting human reader performance.

Image quality metrics derived from displayed images of the penetration phantom are shown in Figs. 10 and 11 (SNR_{disp} is again omitted per Eq. (4)). All metrics were generally lower than those computed from preprocessed images, which is expected as log compression reduces image dynamic range and contrast in order to make the image more readable by a human. CNR_{disp} and SBR_{disp} decreased with depth, although the values began to increase in deep regions where no targets are detectable by inspection (Fig. 10). This is due to remaining display thresholding effects as described previously. All metrics approached slightly higher asymptotes with depth than expected (ideally, CNR approaches zero and SBR approaches one). This may be due to the 50 %-amplitude target ROI mask selection method, which will generally increase measured target amplitude above background even without a target present. Interestingly, the custom system produced relatively constant CNR_{disp} and SBR_{disp} over most detectable targets. This is likely due to higher background amplitude and variation in shallow regions,

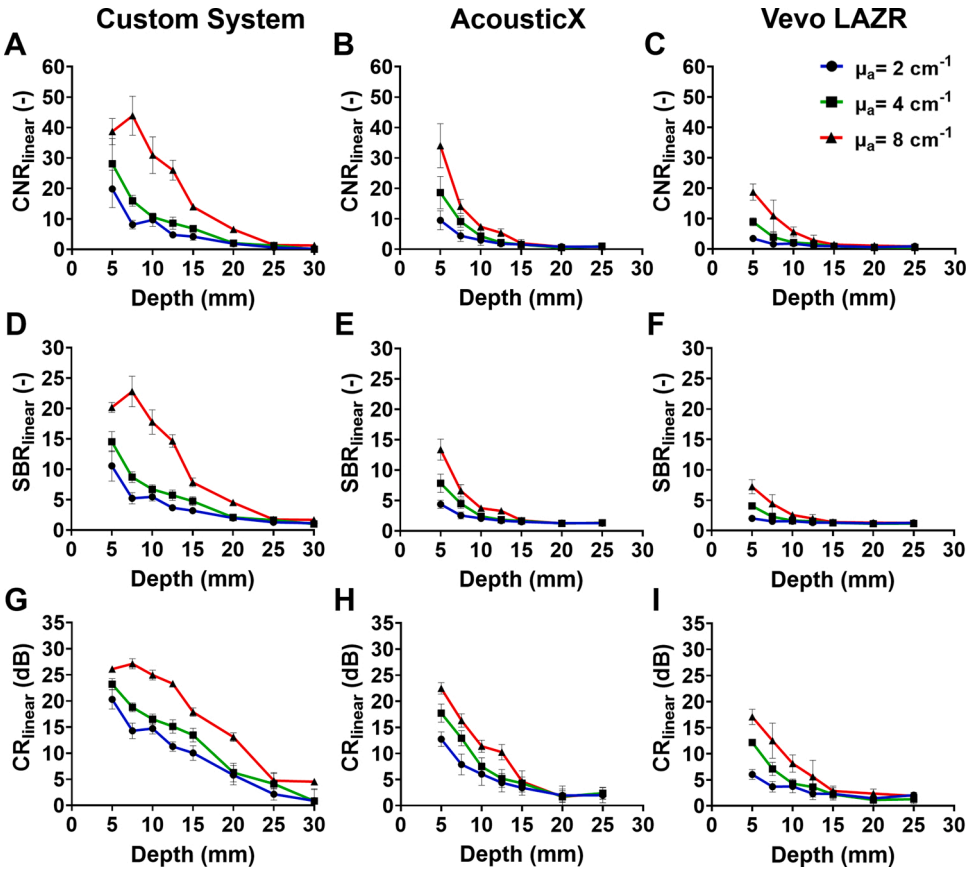

Fig. 8. CNR_{linear} (A-C), SBR_{linear} (D-F), and CR_{linear} (G-I) from linear preprocessed images for each system and target μ_a. SNR_{linear} was omitted, as data showed similar trends with slightly higher values than CNR_{linear} (see Eq. 4).

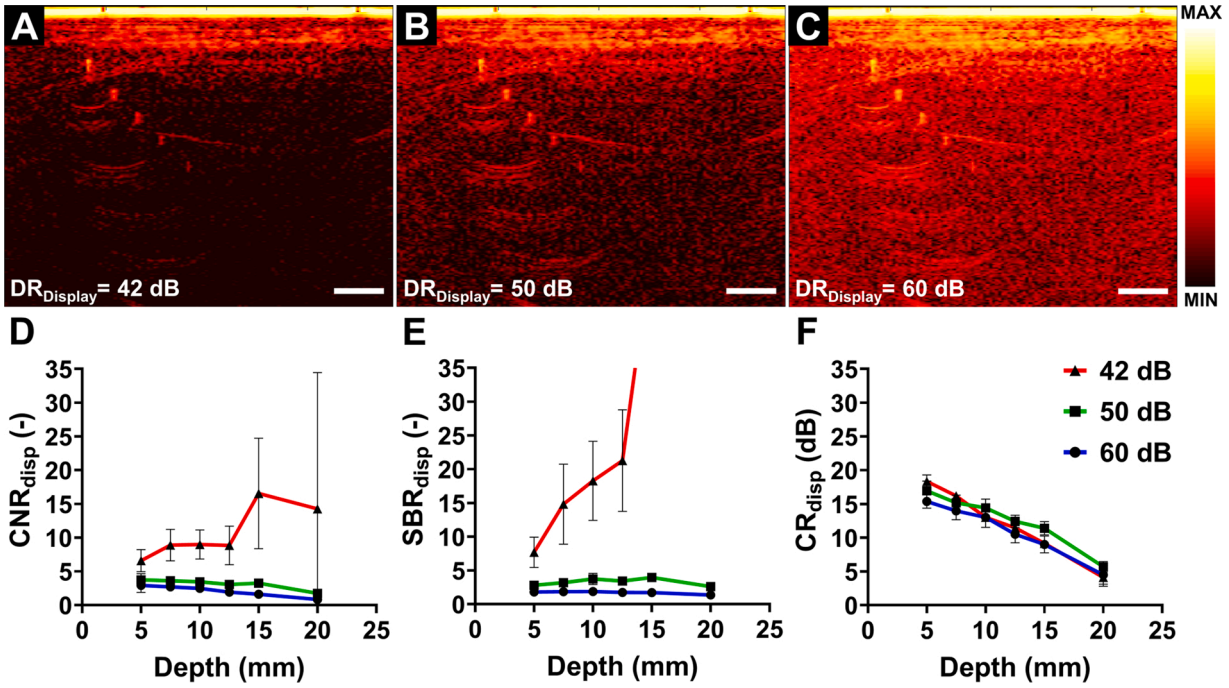

Fig. 9. Custom system images of the penetration phantom with targets at $\mu_a = 4$ cm^{-1} using display dynamic ranges of 42 dB (A), 50 dB (B), or 60 dB (C). Scale bars = 5 mm. Effects of display dynamic range on image quality metrics are shown in D-F.

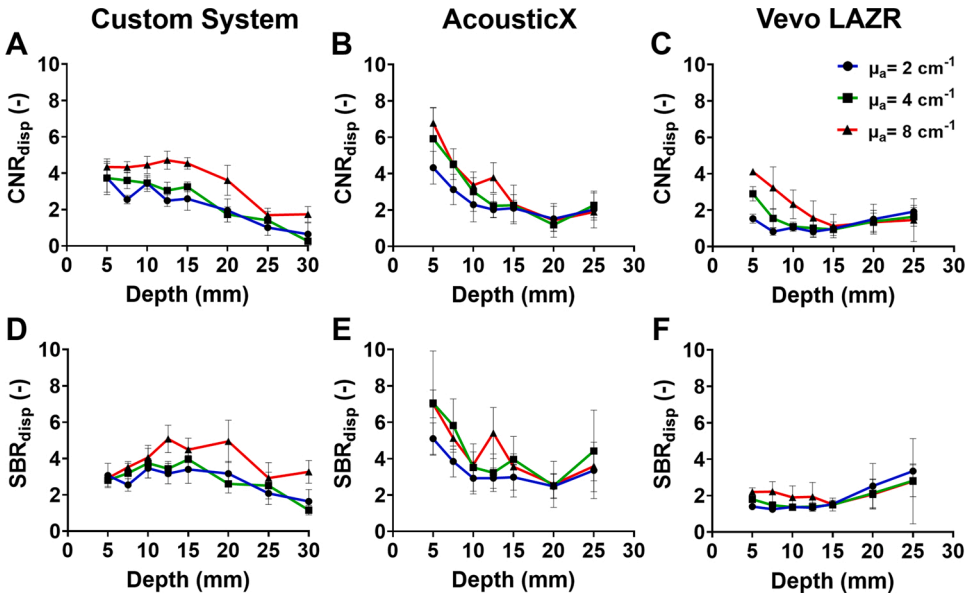

Fig. 10. CNR_{disp} (A-C) and SBR_{disp} (D-F) for the three imaging systems in the penetration phantom at each target absorption level. SNR_{disp} was omitted, as data showed similar trends with slightly higher values than CNR_{linear} (see Eq. 4).

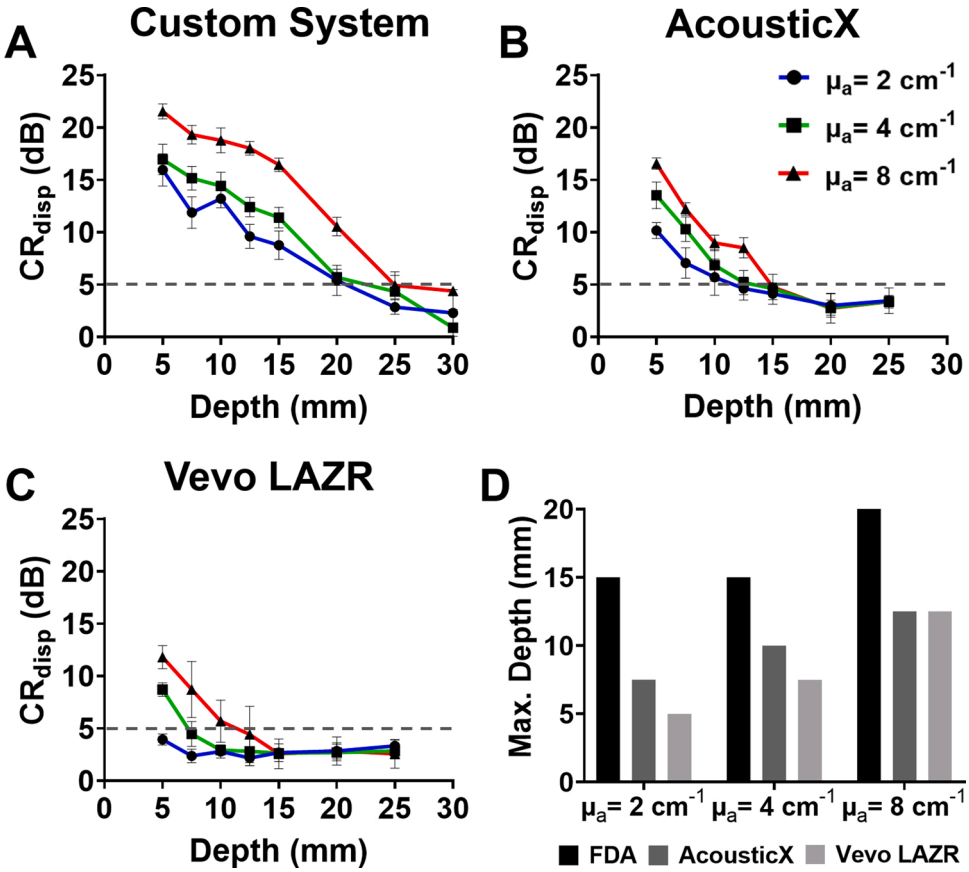

Fig. 11. CR_{disp} vs. depth and target μ_a in the penetration phantom for the custom system (A), AcousticX (B), and Vevo LAZR (C). Max. imaging depth vs. target μ_a is shown in (D).

while the lower amplitude of deeper targets was offset by lower background amplitude and variation in deeper regions.

Of the various image quality metrics computed for displayed images, CR_{disp} was found to correlate best with maximum imaging depth (deepest detectable target) as determined by image inspection (Fig. 11) with an interpolated detection threshold of ~4–6 dB. Maximum imaging depth was highest for the custom system, followed by the AcousticX, then Vevo LAZR. These differences in performance are likely due to different optical and acoustic device design parameters. The custom and Vevo systems use high-energy OPOs to achieve much higher radiant

exposures than the AcousticX. The AcousticX system produces a much lower radiant exposure over a larger beam area, but averages acquisitions at a higher pulse repetition rate [61]. However, this approach may be limited by the minimum detectable pressure produced by a single optical pulse. Transducer parameters may also significantly contribute to observed differences in performance. A strong inverse correlation was observed between maximum imaging depth and transducer center frequency. This may be due to lower phantom α at lower frequencies, as well as target size-dependency of photoacoustic signal amplitude and frequency content. Another possibility is that differences in transducer elevational focusing contribute different out-of-plane signal contributions along the cylindrical targets, which can modify the total signal received. Unfortunately, it was not possible to use transducers with identical parameters across all three systems.

4. Discussion and conclusions

In this study, we developed and characterized a PAA hydrogel-based TMM with stable, widely tunable optical and acoustic properties similar to reported values for soft tissue. We then constructed PAA phantoms suitable for evaluating image quality of PAI systems and that were sufficiently robust for transport. We found that PAA optical and acoustic properties were stable over time and that well-sealed imaging phantoms showed no qualitative signs of desiccation or damage after 6 months of storage at room temperature. This is consistent with the reported service life for Zerdine® hydrogel phantoms of several years [69]. The advantages of PAA hydrogels compared to other available TMMs for PAI include ease of preparation, better mechanical strength/stiffness than common hydrogel-based TMMs, broad dopant compatibility of water, lower preparation temperatures, and lower viscosity during formulation. The disadvantages of PAA include faster dopant settling due to low viscosity, requirements for well-sealed housings to prevent desiccation, reduced gel quality of very high-concentration formulations, and lower mechanical strength than nonaqueous materials such as PVCP and gel wax. Also, while our acoustic characterization data showed low spatial variation (Fig. 3), some heterogeneity might still exist in imaging phantoms [21]. These trade-offs should be carefully considered in selecting TMMs for a given phantom design and application.

Our experimental measurements demonstrated utility of these phantoms for evaluating image quality. Phantom testing of three PAI systems indicated a performance trade-off between spatial resolution and target contrast/imaging depth, which is consistent with our previous phantom-based device comparison study [30]. The purpose of this study was not to rank performance of these PAI devices, as each system is intended for different applications and thus has different performance requirements and design specifications. Rather, this study aimed to demonstrate that the developed TMM and phantoms are suitable for evaluating PAI systems with widely differing design parameters. Additionally, our intent was to highlight the benefit of phantom-based test methods for objective, quantitative, and reproducible characterization of device performance. Phantom-based performance test methods can provide data that illustrates performance trade-offs, elucidates device design consequences, and may help establish performance expectations. Such information can be used to further optimize the design of device hardware or image processing algorithms for a particular application during device development.

Finally, we assessed the suitability of several image quality metrics (SNR, CNR, SBR, and CR) for PAI. We evaluated image quality of both preprocessed linear amplitude images and displayed images, leveraging applicable guidelines from ultrasound standards. Preprocessed image quality is particularly important in PAI as these data preserve linearity of amplitude vs. optical energy deposition and are typically used for quantitative imaging approaches such as oximetry. However, while we could access pre-processed image data for these systems, this may not be true for every user and system. It was thus important to select image quality metrics that yield meaningful insights into performance for images as displayed to a human reader. Test results suggested that CR may correlate best with maximum imaging depth. However, CR may not provide a comprehensive description of image quality under all conditions, for instance in the presence of high, variable background due to clutter or other nearby anatomical features. In such cases, target detectability may be more holistically characterized by noise-based metrics such as CNR, which unlike CR showed sensitivity to changes in image display settings that were qualitatively perceived to modify target detectability. Optimal selection and application of image quality metrics for evaluating photoacoustic images may depend on image content and the intended imaging task or application. Given the current absence of established community consensus on image quality metric selection, it may be most appropriate to evaluate a set of metrics including both CR and CNR. Performance assessment should include analysis of linear images in addition to displayed images.

In conclusion, the PAA-based phantom we developed in this study is stable, robust, and tunable over a range of tissue-relevant optical and acoustic properties. We demonstrated utility of PAA phantoms for image quality assessment of three linear-array PAI systems. The methods proposed here will support much-needed advancements in PAI device design, optimization, and performance assessment. These methods will aid development of standardized PAI test methods that will ultimately facilitate clinical translation of this technology.

Declaration of Competing Interest

The authors declare that there are no conflicts of interest.

Acknowledgments

We gratefully acknowledge funding from the NSF/FDA Scholar-in-Residence program (Awards #1842387 and #1937674). JVJ also acknowledges infrastructure from NIH under grants S10 OD023555 and S10 OD021821. The mention of commercial products, their sources, or their use in connection with material reported herein is not to be construed as either an actual or implied endorsement of such products by the Department of Health and Human Services. This article reflects the views of the authors and should not be construed to represent FDA's views or policies.

References

[1] L.V. Wang, S. Hu, Photoacoustic tomography: in vivo imaging from organelles to organs, Science 335 (2012) 1458–1462.
[2] E.I. Neuschler, R. Butler, C.A. Young, L.D. Barke, M.L. Bertrand, M. Bohm-Velez, S. Destounis, P. Donlan, S.R. Grobmyer, J. Katzen, K.A. Kist, P.T. Lavin, E. V. Makariou, T.M. Parris, K.J. Schilling, F.L. Tucker, B.E. Dogan, A pivotal study of optoacoustic imaging to diagnose benign and malignant breast masses: a new evaluation tool for radiologists, Radiology 287 (2018) 398–412.
[3] S. Manohar, M. Dantuma, Current and future trends in photoacoustic breast imaging, Photoacoustics 16 (2019), 100134.
[4] C.Y. Lin, F. Chen, A. Hariri, C.J. Chen, P. Wilder-Smith, T. Takesh, J.V. Jokerst, Photoacoustic imaging for noninvasive periodontal probing depth measurements, J. Dent. Res. 97 (2018) 23–30.
[5] J. Jo, G. Xu, M. Cao, A. Marquardt, S. Francis, G. Gandikota, X. Wang, A functional study of human inflammatory arthritis using photoacoustic imaging, Sci. Rep. 7 (2017) 15026.
[6] J. Su, A. Karpiouk, B. Wang, S. Emelianov, Photoacoustic imaging of clinical metal needles in tissue, J. Biomed. Opt. 15 (2010), 021309.
[7] S. Gargiulo, S. Albanese, M. Mancini, State-of-the-Art preclinical photoacoustic imaging in oncology: recent advances in Cancer theranostics, Contrast Media Mol. Imaging 2019 (2019) 5080267.
[8] International Electrotechnical Commission, IEC 61391-1:2017, Ultrasonics – Pulse-echo Scanners – Part 1: Techniques for Calibrating Spatial Measurement Systems and Measurement of System Point-spread Function Response, 2017.
[9] M.M. Goodsitt, P.L. Carson, S. Witt, D.L. Hykes, J.M. Kofler Jr., Real-time B-mode ultrasound quality control test procedures. Report of AAPM ultrasound task group No. 1, Med. Phys. 25 (1998) 1385–1406.
[10] J. Rieffel, F. Chen, J. Kim, G. Chen, W. Shao, S. Shao, U. Chitgupi, R. Hernandez, S. A. Graves, R.J. Nickles, P.N. Prasad, C. Kim, W. Cai, J.F. Lovell, Hexamodal imaging with porphyrin-phospholipid-coated upconversion nanoparticles, Adv Mater 27 (2015) 1785–1790.

[11] S.R. Kothapalli, T.J. Ma, S. Vaithilingam, O. Oralkan, B.T. Khuri-Yakub, S. S. Gambhir, Deep tissue photoacoustic imaging using a miniaturized 2-D capacitive micromachined ultrasonic transducer array, IEEE Trans. Biomed. Eng. 59 (2012) 1199–1204.

[12] M. Pramanik, M. Swierczewska, D. Green, B. Sitharaman, L.V. Wang, Single-walled carbon nanotubes as a multimodal-thermoacoustic and photoacoustic-contrast agent, J. Biomed. Opt. 14 (2009), 034018.

[13] E. Zhang, J. Laufer, P. Beard, Backward-mode multiwavelength photoacoustic scanner using a planar Fabry-Perot polymer film ultrasound sensor for high-resolution three-dimensional imaging of biological tissues, Appl. Opt. 47 (2008) 561–577.

[14] J.R. Cook, R.R. Bouchard, S.Y. Emelianov, Tissue-mimicking phantoms for photoacoustic and ultrasonic imaging, Biomed. Opt. Express 2 (2011) 3193–3206.

[15] Y.S. Chen, W. Frey, S. Kim, P. Kruizinga, K. Homan, S. Emelianov, Silica-coated gold nanorods as photoacoustic signal nanoamplifiers, Nano Lett. 11 (2011) 348–354.

[16] A.B. Karpiouk, S.R. Aglyamov, S. Mallidi, J. Shah, W.G. Scott, J.M. Rubin, S. Y. Emelianov, Combined ultrasound and photoacoustic imaging to detect and stage deep vein thrombosis: phantom and ex vivo studies, J. Biomed. Opt. 13 (2008), 054061.

[17] L. Ding, X. Luis Dean-Ben, C. Lutzweiler, D. Razansky, V. Ntziachristos, Efficient non-negative constrained model-based inversion in optoacoustic tomography, Phys. Med. Biol. 60 (2015) 6733–6750.

[18] C. Avigo, N. Di Lascio, P. Armanetti, C. Kusmic, L. Cavigli, F. Ratto, S. Meucci, C. Masciullo, M. Cecchini, R. Pini, F. Faita, L. Menichetti, Organosilicon phantom for photoacoustic imaging, J. Biomed. Opt. 20 (2015) 46008.

[19] J. Levi, S.R. Kothapalli, S. Bohndiek, J.K. Yoon, A. Dragulescu-Andrasi, C. Nielsen, A. Tisma, S. Bodapati, G. Gowrishankar, X. Yan, C. Chan, D. Starcevic, S. S. Gambhir, Molecular photoacoustic imaging of follicular thyroid carcinoma, Clin. Cancer Res. 19 (2013) 1494–1502.

[20] G. Kim, S.W. Huang, K.C. Day, M. O'Donnell, R.R. Agayan, M.A. Day, R. Kopelman, S. Ashkenazi, Indocyanine-green-embedded PEBBLEs as a contrast agent for photoacoustic imaging, J. Biomed. Opt. 12 (2007), 044020.

[21] W. Xia, D. Piras, M. Heijblom, W. Steenbergen, T.G. van Leeuwen, S. Manohar, "Poly(vinyl alcohol) gels as photoacoustic breast phantoms revisited, J. Biomed. Opt. 16 (2011), 075002.

[22] S.E. Bohndiek, S. Bodapati, D. Van De Sompel, S.R. Kothapalli, S.S. Gambhir, Development and application of stable phantoms for the evaluation of photoacoustic imaging instruments, PLoS One 8 (2013), e75533.

[23] G.M. Spirou, A.A. Oraevsky, I.A. Vitkin, W.M. Whelan, Optical and acoustic properties at 1064 nm of polyvinyl chloride-plastisol for use as a tissue phantom in biomedical optoacoustics, Phys. Med. Biol. 50 (2005) N141–N153.

[24] S.L. Vieira, T.Z. Pavan, J.E. Junior, A.A. Carneiro, Paraffin-gel tissue-mimicking material for ultrasound-guided needle biopsy phantom, Ultrasound Med. Biol. 39 (2013) 2477–2484.

[25] E. Maneas, W. Xia, O. Ogunlade, M. Fonseca, D.I. Nikitichev, A.L. David, S.J. West, S. Ourselin, J.C. Hebden, T. Vercauteren, A.E. Desjardins, Gel wax-based tissue-mimicking phantoms for multispectral photoacoustic imaging, Biomed. Opt. Express 9 (2018) 1151–1163.

[26] L.C. Cabrelli, P.I. Pelissari, A.M. Deana, A.A. Carneiro, T.Z. Pavan, Stable phantom materials for ultrasound and optical imaging, Phys. Med. Biol. 62 (2017) 432–447.

[27] J. Laufer, E. Zhang, P. Beard, Evaluation of absorbing chromophores used in tissue phantoms for quantitative photoacoustic spectroscopy and imaging, Ieee J. Sel. Top. Quantum Electron. 16 (2010) 600–607.

[28] S. Manohar, A. Kharine, J.C. van Hespen, W. Steenbergen, T.G. van Leeuwen, Photoacoustic mammography laboratory prototype: imaging of breast tissue phantoms, J. Biomed. Opt. 9 (2004) 1172–1181.

[29] K. Zell, J.I. Sperl, M.W. Vogel, R. Niessner, C. Haisch, Acoustical properties of selected tissue phantom materials for ultrasound imaging, Phys. Med. Biol. 52 (2007) N475–N484.

[30] W.C. Vogt, C. Jia, K.A. Wear, B.S. Garra, T.J. Pfefer, Phantom-based image quality test methods for photoacoustic imaging systems, J. Biomed. Opt. 22 (2017) 1–14.

[31] W.C. Vogt, C. Jia, K.A. Wear, B.S. Garra, T. Joshua Pfefer, Biologically relevant photoacoustic imaging phantoms with tunable optical and acoustic properties, J. Biomed. Opt. 21 (2016), 101405.

[32] C. Jia, W.C. Vogt, K.A. Wear, T.J. Pfefer, B.S. Garra, Two-layer heterogeneous breast phantom for photoacoustic imaging, J. Biomed. Opt. 22 (2017) 1–14.

[33] M. R. Moustafa, B. Zerhouni, "Ultrasonic calibration material and method," U. S. Patent, ed. (Computerized Imaging Reference Systems Inc, 1990).

[34] T. Klinkosz, C.J. Lewa, J. Paczkowski, Propagation velocity and attenuation of a shear wave pulse measured by ultrasound detection in agarose and polyacrylamide gels, Ultrasound Med. Biol. 34 (2008) 265–275.

[35] K. Zell, J.I. Sperl, M.W. Vogel, R. Niessner, C. Haisch, Acoustical properties of selected tissue phantom materials for ultrasound imaging, Phys. Med. Biol. 52 (2007) N475–484.

[36] C. Lafon, V. Zderic, M.L. Noble, J.C. Yuen, P.J. Kaczkowski, O.A. Sapozhnikov, F. Chavrier, L.A. Crum, S. Vaezy, Gel phantom for use in high-intensity focused ultrasound dosimetry, Ultrasound Med. Biol. 31 (2005) 1383–1389.

[37] M.J. Choi, S.R. Guntur, K.I. Lee, D.G. Paeng, A. Coleman, A tissue mimicking polyacrylamide hydrogel phantom for visualizing thermal lesions generated by high intensity focused ultrasound, Ultrasound Med. Biol. 39 (2013) 439–448.

[38] S.R. Guntur, M.J. Choi, An improved tissue-mimicking polyacrylamide hydrogel phantom for visualizing thermal lesions with high-intensity focused ultrasound, Ultrasound Med. Biol. 40 (2014) 2680–2691.

[39] K. Wilson, K. Homan, S. Emelianov, Biomedical photoacoustics beyond thermal expansion using triggered nanodroplet vaporization for contrast-enhanced imaging, Nat. Commun. 3 (2012) 618.

[40] A.S. Hannah, D. VanderLaan, Y.S. Chen, S.Y. Emelianov, Photoacoustic and ultrasound imaging using dual contrast perfluorocarbon nanodroplets triggered by laser pulses at 1064 nm, Biomed. Opt. Express 5 (2014) 3042–3052.

[41] J.L. Sandell, T.C. Zhu, A review of in-vivo optical properties of human tissues and its impact on PDT, J. Biophotonics 4 (2011) 773–787.

[42] International Electrotechnical Commission, IEC 61391-61392:2010, "Ultrasonics – Pulse-echo Scanners – Part 2: Measurement of Maximum Depth of Penetration and Local Dynamic Range, 2010.

[43] W. Oppermann, S. Rose, G. Rehage, The elastic behaviour of hydrogels, Br. Polym. J. 17 (1985) 175–180.

[44] Y.C. Lee, G.D. Fullerton, C. Baiu, M.G. Lescrenier, B.A. Goins, Preclinical multimodality phantom design for quality assurance of tumor size measurement, BMC Med. Phys. 11 (2011) 1.

[45] E.L. Madsen, G.R. Frank, T.A. Krouskop, T. Varghese, F. Kallel, J. Ophir, Tissue-mimicking oil-in-gelatin dispersions for use in heterogeneous elastography phantoms, Ultrason. Imaging 25 (2003) 17–38.

[46] J.R. Cook, R.R. Bouchard, S.Y. Emelianov, Tissue-mimicking phantoms for photoacoustic and ultrasonic imaging, Biomed. Opt. Express 2 (2011) 3193–3206.

[47] M.O. Culjat, D. Goldenberg, P. Tewari, R.S. Singh, A review of tissue substitutes for ultrasound imaging, Ultrasound Med. Biol. 36 (2010) 861–873.

[48] K.A. Wear, Measurements of phase velocity and group velocity in human calcaneus, Ultrasound Med. Biol. 26 (2000) 641–646.

[49] K.A. Wear, Mechanisms of interaction of ultrasound with cancellous bone: a review, IEEE Trans. Ultrason. Ferroelectr. Freq. Control 67 (2020) 454–482.

[50] S. Maruvada, Y. Liu, P. Gammell, K. Wear, Broadband characterization of plastic and high intensity therapeutic ultrasound phantoms using time delay spectrometry-With validation using Kramers-Kronig relations, J. Acoust. Soc. Am. 143 (2018) 3365.

[51] L.E. Kinsler, A.R. Frey, A.B. Coppens, J.V. Sanders, Fundamentals of Acoustics, John Wiley and Sons, 1982.

[52] X. Dai, H. Yang, H. Jiang, In vivo photoacoustic imaging of vasculature with a low-cost miniature light emitting diode excitation, Opt. Lett. 42 (2017) 1456–1459.

[53] H.G. Akarcay, S. Preisser, M. Frenz, J. Ricka, Determining the optical properties of a gelatin-TiO_2 phantom at 780 nm, Biomed. Opt. Express 3 (2012) 418–434.

[54] S.A. Prahl, M.J.C. Van Gemert, A.J. Welch, Determining the optical-properties of turbid media by using the adding-doubling method, Pure Appl. Opt. J. Eur. Opt. Soc. Part A 32 (1993) 559–568.

[55] S.A. Prahl, Inverse Adding-Doubling, 2020. September 8, https://omlc.org/software/iad/.

[56] P. Ghassemi, J. Wang, A.J. Melchiorri, J.C. Ramella-Roman, S.A. Mathews, J. C. Coburn, B.S. Sorg, Y. Chen, T.J. Pfefer, Rapid prototyping of biomimetic vascular phantoms for hyperspectral reflectance imaging, J. Biomed. Opt. 20 (2015), 121312.

[57] M. Fonseca, B. Zeqiri, P.C. Beard, B.T. Cox, Characterisation of a phantom for multiwavelength quantitative photoacoustic imaging, Phys. Med. Biol. 61 (2016) 4950–4973.

[58] G.M. Hale, M.R. Querry, Optical constants of water in the 200-nm to 200-microm wavelength region, Appl. Opt. 12 (1973) 555–563.

[59] M.L. Byron, E.A. Variano, Refractive-index-matched hydrogel materials for measuring flow-structure interactions, Exp. Fluids 54 (2013).

[60] H.K. Walker, W.D. Hall, J.W. Hurst, Clinical Methods: The History, Physical and Laboratory Examinations, Butterworth-Heinemann, St. Louis, MO, 1990.

[61] A. Hariri, J. Lemaster, J. Wang, A.S. Jeevarathinam, D.L. Chao, J.V. Jokerst, The characterization of an economic and portable LED-based photoacoustic imaging system to facilitate molecular imaging, Photoacoustics 9 (2018) 10–20.

[62] A. Hariri, J. Wang, Y. Kim, A. Jhunjhunwala, D.L. Chao, J.V. Jokerst, In vivo photoacoustic imaging of chorioretinal oxygen gradients, J. Biomed. Opt. 23 (2018) 1–8.

[63] R.E. Daigle, Ultrasound Imaging System With Pixel Oriented Processing, Verasonics Inc., 2015.

[64] J.M. Thijssen, G. Weijers, C.L. de Korte, Objective performance testing and quality assurance of medical ultrasound equipment, Ultrasound Med. Biol. 33 (2007) 460–471.

[65] J. Yan, J. Schaefferkoetter, M. Conti, D. Townsend, A method to assess image quality for low-dose PET: analysis of SNR, CNR, bias and image noise, Cancer Imaging 16 (2016) 26.

[66] J.J. Dahl, D. Hyun, M. Lediju, G.E. Trahey, Lesion detectability in diagnostic ultrasound with short-lag spatial coherence imaging, Ultrason. Imaging 33 (2011) 119–133.

[67] X. Zhou, N. Akhlaghi, K.A. Wear, B.S. Garra, T.J. Pfefer, W.C. Vogt, Evaluation of fluence correction algorithms in multispectral photoacoustic imaging, Photoacoustics 19 (2020), 100181.

[68] H.H. Barrett, K.J. Myers, C. Hoeschen, M.A. Kupinski, M.P. Little, Task-based measures of image quality and their relation to radiation dose and patient risk, Phys. Med. Biol. 60 (2015) R1–R75.

[69] CIRS Inc., www.cirsinc.com/support/faq. September 8, 2020.

Ali Hariri is a PhD candidate in the Nanoengineering Department at UCSD. He got his M.S. degree and B.S degree in Biomedical Engineering from Sharif University of Technology and Amirkabir University of Technology in Iran. He worked on developing different configurations of photoacoustic imaging technique including computed tomography and microscopy (both acoustic and optical resolution). He also worked on measuring the functional connectivity in resting state using fMRI images on methamphetamine dependence.

Jesse V. Jokerst is an Associate Professor in the Department of NanoEngineering at UC San Diego. Dr. Jokerst graduated *cum laude* from Truman State University in 2003 with a B.S. in Chemistry and completed a Ph.D. in Chemistry at The University of Texas at Austin in 2009. Jesse was a postdoc at Stanford Radiology from 2009 to 2013 and was an Instructor in that same department from 2013–2015. Jesse started at UCSD in July of 2015, and he has received the NIH K99/R00 Pathway to Independence Award, the NIH New Innovator Award, the NSF CAREER Award, and Stanford Radiology Alumni of the Year Award. He is the PI of seven active NIH grants, three NSF grants, and serves on the Editorial Advisory Board of *ACS Applied Nano Materials* and *Nanoscale.*

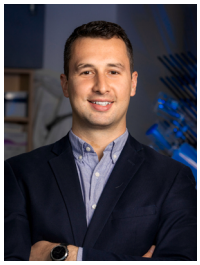

Jorge Palma-Chavez is a postdoctoral scholar in the in the Department of NanoEngineering at UC San Diego and a NSF Scholar-in-Residence fellow at FDA. Dr. Palma-Chavez graduated from Universidad La Salle in 2013 with a B.S. in Electrical Engineering. He earned his PhD in Biomedical Engineering from Texas A&M University, where he developed contrast agents for optical imaging techniques and designed vascular-targeted drug delivery platforms. He is currently working on tissue-mimicking phantoms for characterization and image quality assessment of photoacoustic imaging systems.

T. Joshua Pfefer received his PhD in biomedical engineering from the University of Texas at Austin and trained as a research fellow at the Wellman Laboratories of Photomedicine. In 2000, he joined the FDA, where he is the leader of the Optical Diagnostic Devices Laboratory. His research focuses on elucidating light-tissue interactions of emerging technologies and developing new methods to improve and standardize testing. In 2018, he was named a fellow of SPIE for contributions to biophotonics.

William C. Vogt received his BS degree in mechanical engineering from the University of Massachusetts Amherst in 2009 and his PhD in biomedical engineering from Virginia Polytechnic Institute and State University in 2013. Since joining the FDA in 2013, he has been conducting regulatory science to develop tools and test methods for evaluating the safety and effectiveness of photoacoustic imaging devices. His research interests include photoacoustic imaging, tissue phantoms, nanoparticles, standardization, and biophotonic medical device characterization and evaluation.

Keith A. Wear received his BA degree in applied physics from the University of California, San Diego and his MS and PhD degrees in applied physics from Stanford University. He is a research physicist at the FDA. He is an associate editor in chief of IEEE Transactions on Ultrasonics, Ferroelectrics, and Frequency Control. He is an associate editor of the Journal of the Acoustical Society of America and Ultrasonic Imaging. He is a fellow of the Acoustical Society of America, the American Institute for Medical and Biological Engineering, and the American Institute of Ultrasound in Medicine